Chemical Engineering Journal 483 (2024) 149249

Contents lists available at ScienceDirect

Chemical Engineering Journal

journal homepage: www.elsevier.com/locate/cej

Enzymatic metal oxide/nanoparticle heterojunctions with mutually reinforced bifunctional chemotherapies for combating drug-resistant bacteria

Qian Zhou [a,1], Ting Wang [b,1], Zhenyu Xing [b], Raul D. Rodriguez [c], Liang Cheng [d], Yang Gao [e,*], Qiu Chen [a,*], Chong Cheng [b,*]

[a] Department of Endocrinology, Hospital of Chengdu University of Traditional Chinese Medicine, Chengdu, Sichuan 610072, China
[b] College of Polymer Science and Engineering, State Key Laboratory of Polymer Materials Engineering, Sichuan University, Chengdu 610065, China
[c] Tomsk Polytechnic University, 30 Lenin Avenue, Tomsk 634050, Russia
[d] Department of Materials Science and Engineering, The Macau University of Science and Technology, Taipa, Macau
[e] Department of Medical Ultrasound, West China Hospital, Sichuan University, Chengdu 610041, China

ARTICLE INFO

Keywords:
Artificial biocatalysts
Catalytic ROS production
Bifunctional chemotherapies
Antibacterial
Wound disinfection

ABSTRACT

Non-healing diabetic wounds caused by continuous bacterial infections comprise one of the main complications in individuals with diabetes, posing a significant risk that often results in limb amputation. The growing concern of antibiotic resistance has prompted the exploration of non-antibiotic strategies to combat bacteria effectively. Here, an Ag-doped V_2O_5 (Ag-V_2O_5) heterojunction biocatalyst is designed to act as an artificial enzyme for the catalytic treatment of bacterial infections in rats' skin wounds through the bifunctional chemotherapies of reactive oxygen species (ROS) and Ag^+. Experimental analyses confirm that the Ag-V_2O_5 catalyst exhibits exceptional peroxidase (POD)-mimetic performance, with a V_{max} value of 2.66 μM s^{-1} and a turnover number of 200.88×10^{-3} s^{-1}, surpassing most POD-mimetic catalysts. Furthermore, the Ag-V_2O_5 exhibits remarkable Ag^+ leaching capabilities, attributed to its high $V^{5+}/V^{4+/3+}$ ratio and weak metal-support interactions. Benefiting from the bifunctional chemotherapies of ROS and Ag^+, the Ag-V_2O_5 exhibits a low minimal inhibition concentration (32 μg/mL Ag-V_2O_5) against *S. aureus* and effectively promotes wound healing. The innovative strategy of bifunctional chemotherapies on valence-modulated Ag^+ release and ROS-catalysis represents a significant leap forward in chronic wound treatment, inspiring future breakthroughs in biomedical therapeutics based on Ag^+ and ROS.

1. Introduction

Diabetic ulcer with an inflammatory and refractory wound is a complication of diabetes that significantly increases the amputation rate and mortality of diabetic patients [1–3]. The limited self-recovery capacity caused by persistent bacterial infection and the complexity and susceptibility of the lesion area presents significant challenges for diabetic ulcer therapy [4–7]. Traditional treatments, including wound dressings, have limited therapeutic efficacy and poor antimicrobial properties [8–11]. The efficacy of broad-spectrum antibiotics in treating severe bacterial infections in chronic wounds is significantly undermined by the rapid development of bacterial resistance and the uncertainty surrounding the most effective antibiotic protocols and clinical applications [12–16]. In response to these critical challenges, researchers worldwide are actively seeking to develop more effective and potent therapies and antimicrobial agents with low toxicity profiles to accelerate the healing of bacterially infected wounds [17–20].

The emergence of nanocomposites has sparked a paradigm shift, combining responsive chemical platforms with bioactive nanoparticles to wield diverse therapeutic properties [21–26]. These nanoparticles, including gold (Au), silver (Ag), and copper (Cu), exhibit antimicrobial activities that can be harnessed in the treatment of infectious diabetic wounds through chemotherapies [27–29]. Notably, Ag nanoparticles (AgNPs) have emerged as high-performance broad-spectrum

* Corresponding authors.
E-mail addresses: yang.gao0917@scu.edu.cn (Y. Gao), chenqiu1005@cdutcm.edu.cn (Q. Chen), chong.cheng@scu.edu.cn (C. Cheng).
[1] These authors contributed equally to this paper.

https://doi.org/10.1016/j.cej.2024.149249
Received 12 November 2023; Received in revised form 8 January 2024; Accepted 30 January 2024
Available online 2 February 2024

antimicrobial agents [30–32]. AgNPs' antibacterial activity primarily stems from their ability to interact with phosphorus and sulfur-containing compounds, such as DNA and proteins, altering their structure [33–36]. Additionally, AgNPs can release Ag^+ ions and disrupt the respiratory chain in the inner membrane, which in turn affect bacterial metabolic pathways, induce membrane dysfunction, block transmembrane/intracellular signaling, and even trigger bacteria death [37–39]. Despite these benefits, the use of Ag poses challenges due to its potential toxicity and high cost when used in large quantities [40–44]. Therefore, it is necessary to develop composite catalysts that harness the antimicrobial efficacy of silver while minimizing its usage to mitigate toxicity and costs.

Currently, the use of reactive oxygen species (ROS)-generating platforms to deliver Ag has shown promise in reducing Ag dosage requirements through a bifunctional biocidal interaction between ROS and Ag^+ [45]. However, most ROS-generating platforms exhibit strong interactions with Ag, resulting in low Ag^+ release efficiency and poor biocidal performance [46,47]. Thus, the current challenge in chemotherapeutic sterilization lies in the ab initio design of chemically responsive structures that can efficiently generate ROS, while simultaneously minimizing the amount of Ag utilized and facilitating the release of Ag^+ [46,48–51].

To address this challenge, we present here an enzymatic silver-doped vanadium oxide (Ag-V_2O_5) heterojunction with bifunctional chemotherapies for combating drug-resistant bacterial infections. The motivation for this research is based on three key factors: (1) the fully filled electron orbitals of V in V_2O_5 hinder electron transfer from Ag through the bridging oxygen bond, resulting in weak interaction between the V_2O_5 substrate and Ag [52,53]; (2) this weak metal-substrate interaction promotes the efficient release of bactericidal Ag^+ ions; (3) our Ag-V_2O_5 heterojunction demonstrates exceptional ROS generation activity when exposed to H_2O_2, achieving a maximum reaction velocity (V_{max}) of 2.66 μM s^{-1} and a turnover value of 200.88×10^{-3} s^{-1}, surpassing most MOFs, single-atom enzyme mimics, metal oxides, and metal nanoparticles. The synergistic action of Ag^+ and ROS provides the Ag-V_2O_5 system a minimal inhibitory concentration of only 32 μg/mL against *S. aureus*, and its

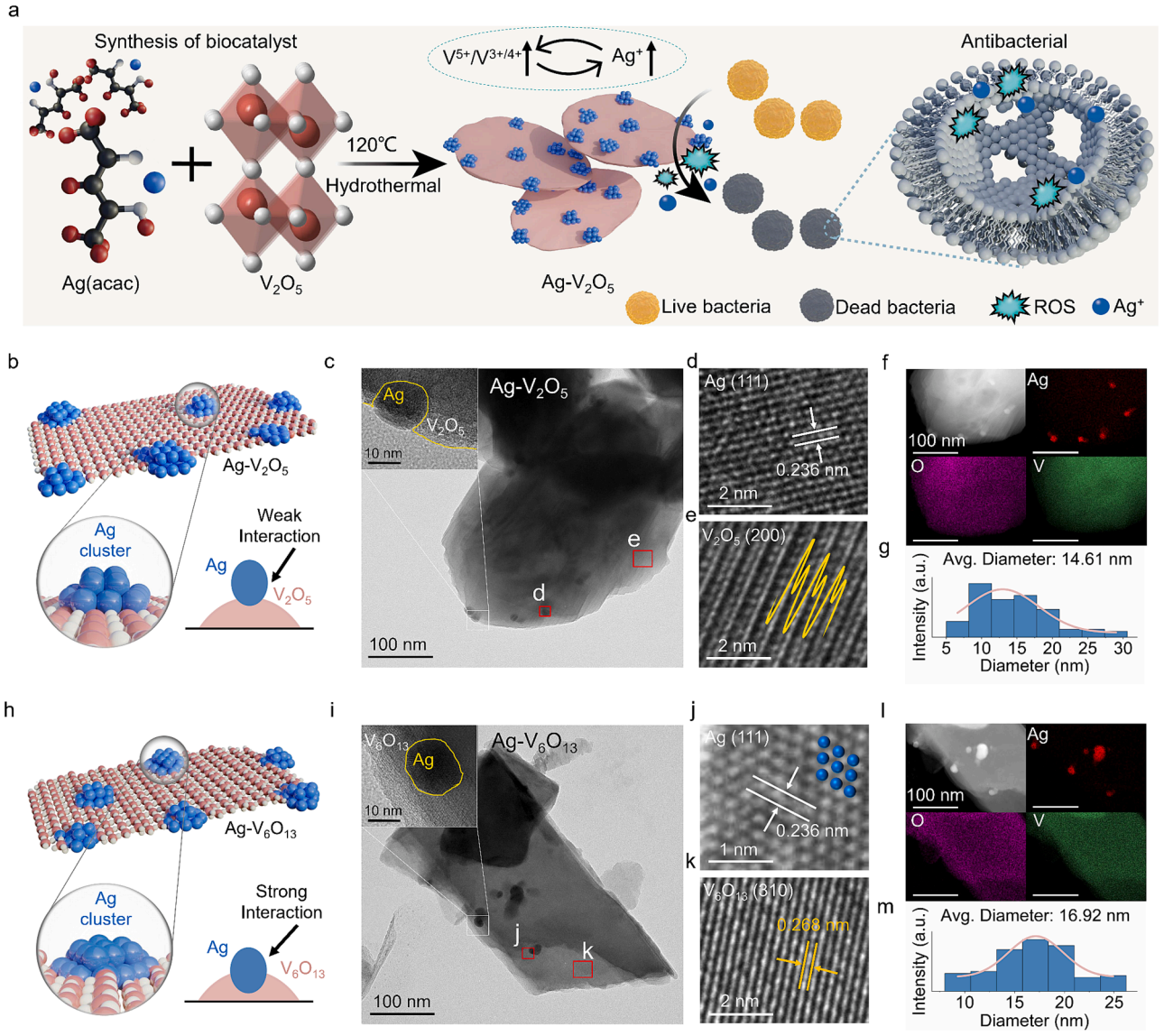

Fig. 1. Synthesis and morphological characterizations of the Ag-V_2O_5 and Ag-V_6O_{13} biocatalysts. (a) Schematic illustration of the preparation process for Ag-V_2O_5. (b) Structure diagram of Ag-V_2O_5. Atomic color coding in the structure: Ag, blue; V, pink; and O, gray. (c) TEM images and (d-e) HR-TEM images of Ag-V_2O_5 biocatalyst. (f) HAADF-STEM and corresponding elemental mapping of Ag-V_2O_5. (g) Distribution graph of Ag particle size in Ag-V_2O_5. (h) Structure diagram of Ag-V_6O_{13}. Atomic color coding in the structure: Ag, blue; V, pink; and O, gray. (i) TEM image and (j-k) HR-TEM images of Ag-V_6O_{13} biocatalyst. (l) HAADF-STEM and corresponding elemental mapping of Ag-V_6O_{13}. (m) Distribution graph of Ag particle size in Ag-V_6O_{13}.

wound healing efficacy rivals that of vancomycin in rat models. With its dual-action therapeutic potential and efficacy, our heterojunction system is a strong candidate for clinical applications, opening a new avenue for advancing the treatment and recovery of infected wounds.

2. Results and discussion

2.1. Characterization of artificial antibacterial catalyst

To achieve massive ROS and Ag^+ generation, we have created an Ag nanoparticle doped V_2O_5 heterojunction (Ag-V_2O_5) as a highly efficient artificial antibacterial catalyst. This catalyst is characterized by a weak interaction between Ag and V_2O_5, optimizing its efficiency. The synthesis of pristine Ag-V_2O_5 was achieved by a simple hydrothermal process at 120 ℃ via the reaction of Ag acetylacetonate ([CH_3COCH=C(O-)CH_3]Ag) with V_2O_5 (Fig. 1a and b). By changing the amount of Ag acetylacetonate, different ratios of Ag-doped V_2O_5 (denoted as Ag-V_2O_5 1:20, Ag-V_2O_5 1:60, and Ag-V_2O_5 1:100) were obtained. The Ag-V_2O_5 1:60 variant displays the best catalytic dynamics for ROS production and is the focal point of our subsequent analyses (Fig. S1, Supporting Information). It is important to note that, unless stated otherwise, references to Ag-V_2O_5 in this study refer to the Ag-V_2O_5 1:60 sample. Moreover, for comparison, we prepared a control sample consisting of Ag nanoparticles on V_6O_{13} sheets biocatalyst (Ag-V_6O_{13}) using the same one-pot synthesis. This involved the reduction of V_2O_5 to V_6O_{13} at 600 ℃ under a hydrogen atmosphere as a reducing medium, followed by the hydrothermal addition of Ag acetylacetonate (Fig. 1h).

Scanning electron microscopy (SEM) revealed that both the synthesized Ag-V_2O_5 and Ag-V_6O_{13} catalysts have a submicron-sheet shape (Figs. S2-S3, Supporting Information). Transmission electron

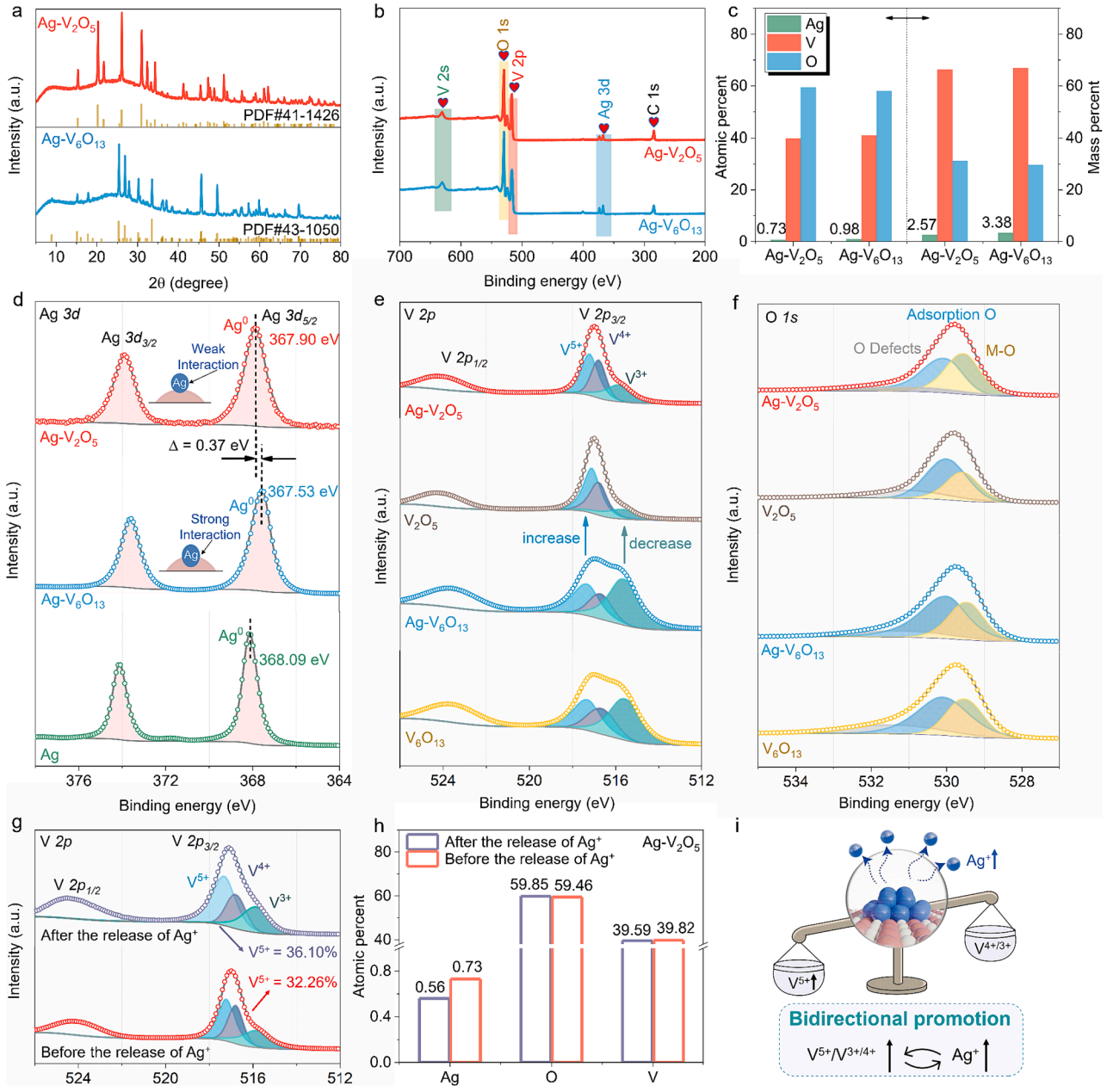

Fig. 2. Detailed coordinated structure analysis of artificial enzyme catalysts. (a) X-ray diffraction (XRD) of Ag-V_2O_5 and Ag-V_6O_{13}. (b) The X-ray photoelectron spectroscopy (XPS) survey of Ag-V_2O_5 and Ag-V_6O_{13}. (c) Atomic and mass ratio of different catalysts. The high-resolution XPS of (d) Ag *3d*, (e) V *2p*, and (f) O *1s* of different catalysts. (g) V *2p* XPS spectra and (h) atomic ratio of Ag-V_2O_5 before and after Ag^+ release. (i) Mutually reinforced function between the release of Ag^+ and the proportion of V^{5+}.

microscopy (TEM) results further show the heterostructure of both catalysts, where Ag nanoparticles are sporadically distributed over V_2O_5 and V_6O_{13} (Fig. 1c and i), in comparison to V_2O_5 and V_6O_{13} submicron-sheet (Figs. S4-S5, Supporting Information). It is noteworthy that Ag nanoparticles exhibit partial surface confinement in Ag-V_2O_5, suggesting a weak interaction between Ag and V_2O_5. In contrast, the Ag-V_6O_{13} sample reveals a complete entrapment of Ag nanoparticles within the V_6O_{13} lattice. High-resolution TEM (HR-TEM) reveals the lattice spacings of Ag nanoparticles as approximately 0.237 nm, matching the (111) planes of Ag (Fig. 1d and j). The crystal faces viewed along the (200) and (310) plane of V_2O_5 and V_6O_{13} in Ag-V_2O_5 and Ag-V_6O_{13}, respectively, match well with these measurements, as shown in Fig. 1e and k. The element mapping via high-angle annular dark field-STEM (HAADF-STEM) imaging shows that V and O elements are uniformly distributed, while Ag is aggregated on the layered Ag-V_2O_5 and Ag-V_6O_{13} (Fig. 1f and l). Furthermore, the particle size statistics in Fig. 1g and Fig. 1m confirm that the average diameter of Ag nanoparticles is about 14.61 nm for Ag-V_2O_5 and 16.92 nm for Ag-V_6O_{13} (Figs. S4-S5, Supporting Information). These findings confirm that within the Ag-V_2O_5 system, Ag nanoparticles are primarily located on the surface of V_2O_5, which is conducive to the release of Ag^+ ions. Conversely, the Ag-V_6O_{13} system shows a more profound incorporation of Ag nanoparticles into the V_6O_{13} lattice, suggesting a stronger interaction that could affect the release and therapeutic efficacy of Ag^+.

X-ray diffraction (XRD) analysis confirmed the successful synthesis of the artificial enzyme-mimetic catalysts Ag-V_2O_5 and Ag-V_6O_{13}, as depicted in Fig. 2a. We used X-ray photoelectron spectroscopy (XPS) to explore the chemical compositions, surface oxidation states, and electronic structure of these catalysts. Fig. 2b displays the XPS survey spectra, revealing the presence of V, O, and Ag, corroborating the results obtained from energy-dispersive X-ray spectroscopy. Surface composition analysis in Fig. 2c indicates that the atomic ratio and mass ratio of Ag in Ag-V_2O_5 are lower than those in Ag-V_6O_{13}, while the amount of O elements in Ag-V_2O_5 is higher than that in Ag-V_6O_{13}. This suggests differing degrees of silver incorporation and oxidation states between the two. Furthermore, the Ag $3d_{5/2}$ binding energies, as shown in

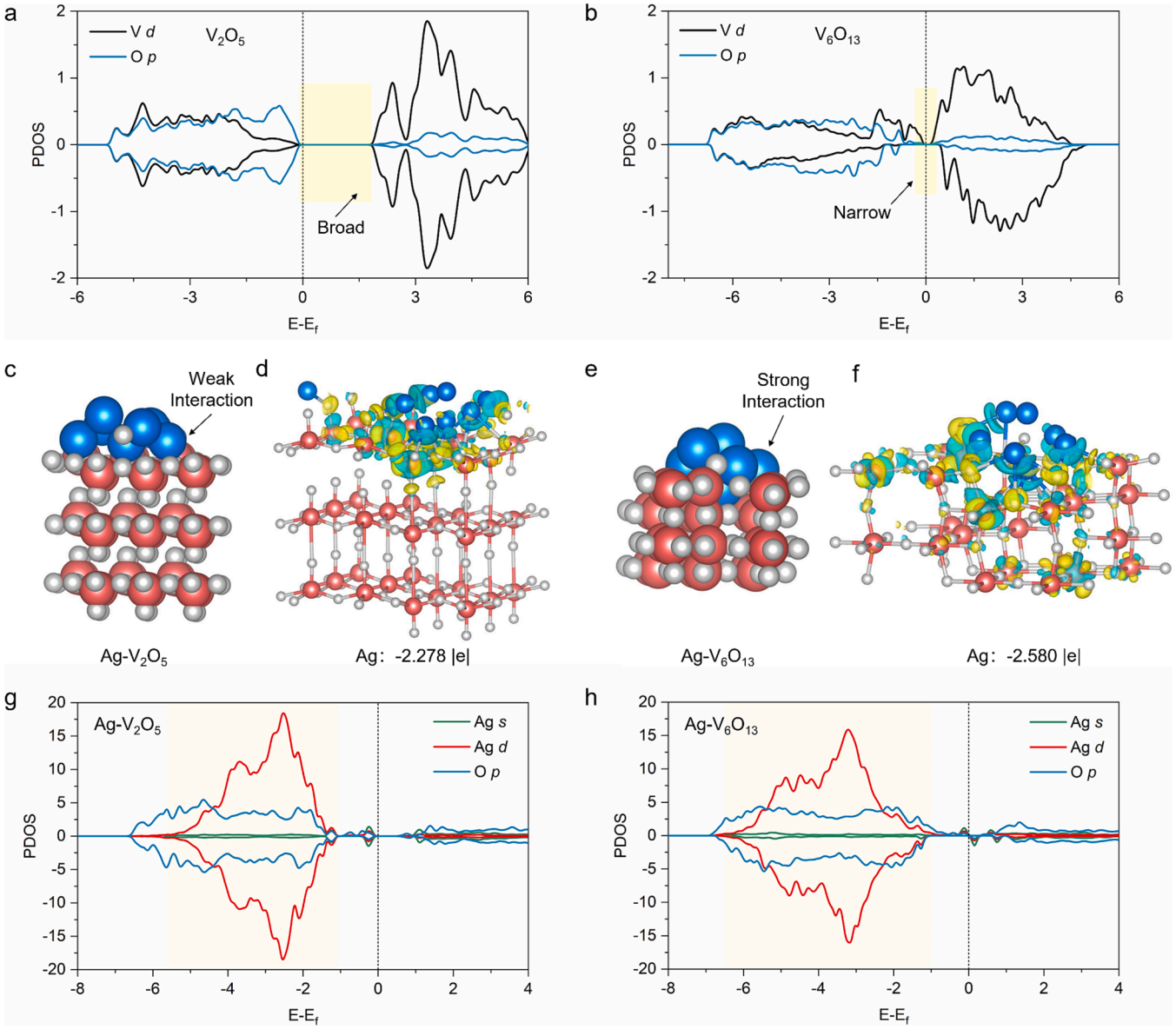

Fig. 3. Theoretical calculations of electronic structure analysis of artificial enzyme catalysts. PDOS analysis of the V *4d* orbital and O *2p* orbital for (a) V_2O_5 and (b) V_6O_{13}. Crystal structure analysis for (c) Ag-V_2O_5 and (e) Ag-V_6O_{13}, and differential charge density analysis of (d) Ag-V_2O_5 and (f) Ag-V_6O_{13} (yellow and cyan represent charge accumulation and depletion, respectively, with a cutoff value of 0.006 e·Bohr^{-3} for the density-difference isosurface). PDOS analysis of the Ag *s* orbital, Ag *4d* orbital, and O *2p* orbital for (g) Ag-V_2O_5 and (h) Ag-V_6O_{13}.

Fig. 2d, are lower compared to Ag nanoparticles, indicating interactions between Ag nanoparticles and the V_2O_5 and V_6O_{13} substrate materials. Notably, the smaller binding energy shift in Ag-V_2O_5 compared to Ag-V_6O_{13} indicates a weaker interaction between Ag and V_2O_5. The V *2p* XPS spectrum of Ag-V_2O_5 exhibits characteristic peaks at 515.48 eV, 516.78 eV, and 517.38 eV, corresponding to V^{3+} *2p3/2*, V^{4+} *2p3/2*, and V^{5+} *2p3/2*, respectively (Fig. 2e). The Ag-V_2O_5 biocatalyst shows a decrease in low-valence V (V^{4+} and V^{3+}) and an increase in V^{5+} compared to Ag-V_6O_{13}. High-resolution spectra demonstrate that the binding energy and intensity of O *1s* in Ag-V_2O_5 are comparable to those of Ag-V_6O_{13} (Fig. 2f). Moreover, V *2p* XPS spectra of Ag-V_2O_5, following extended immersion in solution, demonstrate that the release of Ag^+ ions results in an increase in the V valence state (Fig. 2g and h). This observation implies a reciprocal correlation between the release of Ag^+ and the proportion of V^{5+}. These results suggest that the substantial presence of V^{5+} in V_2O_5 leads to the complete occupation of V's orbital electrons, resulting in a reduced ability for V to capture Ag electrons through bridge-oxygen bonding. Consequently, this weakens the interaction between Ag nanoparticles and the V_2O_5 substrate, facilitating the release of Ag^+ (Fig. 2i).

We conducted density functional theory (DFT) calculations to further investigate the mechanisms underlying the differential interactions of Ag nanoparticles with the V_2O_5 and V_6O_{13} substrates. Initially, we analyzed the electronic structure of the substrates, revealing that the V_2O_5 substrate possesses a broad band gap, which impedes its interaction with Ag nanoparticles (Fig. 3a). Conversely, the V_6O_{13} substrate features a smaller band gap, suggesting heightened reactivity and facilitating electron transfer, potentially resulting in stronger interactions with Ag nanoparticles (Fig. 3b). Subsequently, we constructed models of V_2O_5- and V_6O_{13}-loaded Ag nanoparticles. Our findings indicate that the V in V_2O_5, being in a saturated coordination state, weakly interacts with the surface Ag nanoparticles (Fig. 3c). In contrast, the V in V_6O_{13}, existing in an unsaturated coordination state, exhibits stronger interactions with Ag nanoparticles, resulting in Ag nanoparticles inside the lattice of V_6O_{13} (Fig. 3e). Differential charge density analysis reveals a greater loss of electrons from Ag in the Ag-V_6O_{13} structure compared to the Ag-V_2O_5 structure, consistent with experimental results and supporting the strong interaction between Ag nanoparticles and V_6O_{13} (Fig. 3d and f). Furthermore, the partial density of states (PDOS) demonstrates that the Ag *3d* orbitals in Ag-V_6O_{13} exhibit greater overlap with the O *2p* orbitals, indicating a stronger interaction between Ag and V_6O_{13} compared to Ag-V_2O_5 (Fig. 3g and h).

2.2. Enzyme-mimetic and Ag^+ generation activity evaluations

The ability of Ag-V_2O_5 and Ag-V_6O_{13} biocatalysts to transform hydrogen peroxide (H_2O_2) into reactive oxygen species by POD-mimetic activity was evaluated using the colorimetric probe, 3,3′,5,5′-

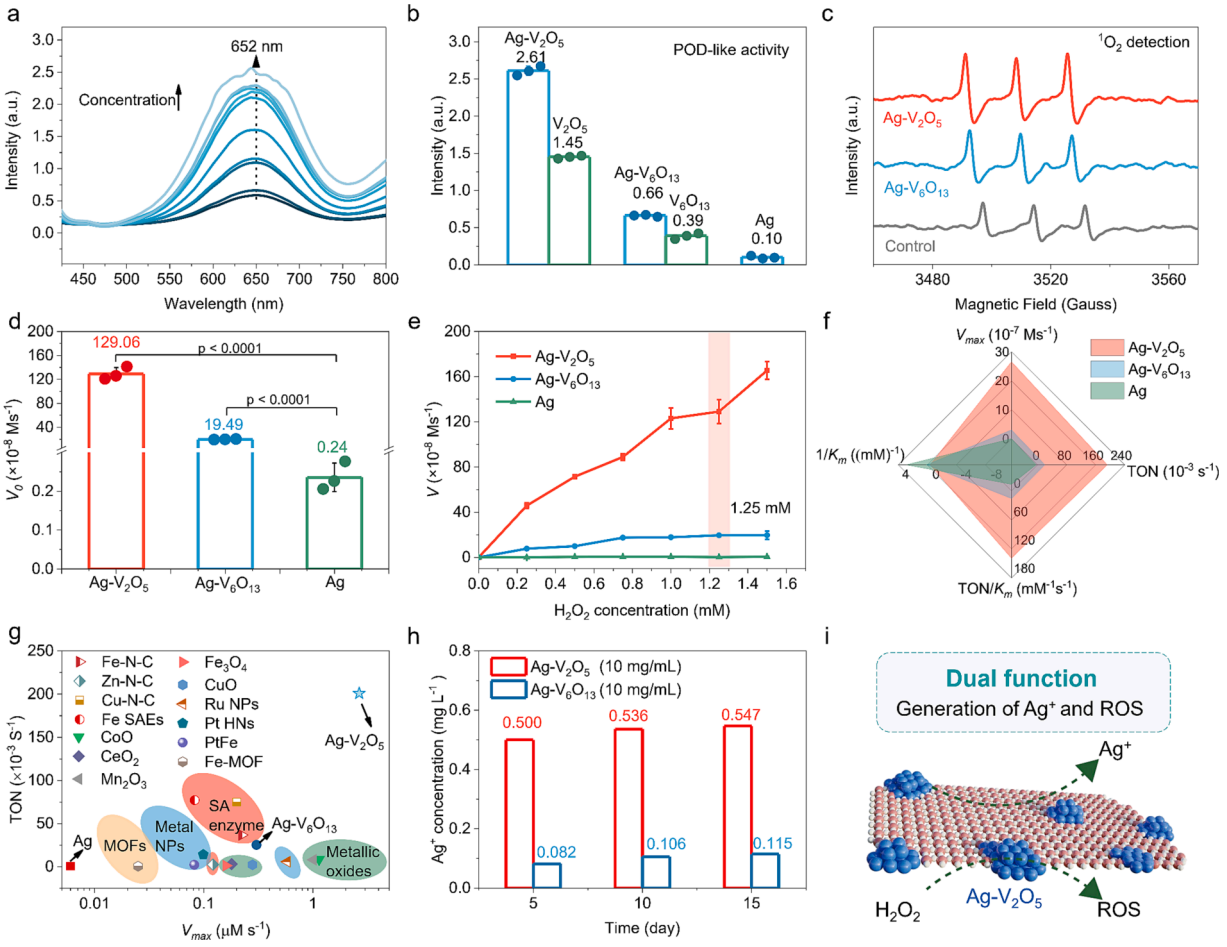

Fig. 4. Enzyme-mimetic and Ag^+ generation activity evaluations. (a) Concentration-dependent POD-mimetic activity. (b) POD-mimetic activity of different catalysts (n = 3 independent experiments, data are presented as mean ± SD). (c) DMPO spin-trapping EPR spectra of different catalysts with $^1O_2$ radical scavenger in DMSO solution. (d) Initial reaction rate of POD-mimetic activity of Ag-V_2O_5, Ag-V_6O_{13}, and Ag. (e) Curves of V_0 with H_2O_2 concentration of different samples. (f) V_{max}, $1/K_m$, TON/K_m and TON values of Ag-V_2O_5, Ag-V_6O_{13}, and Ag. (g) Comparison of the TON and V_{max} values with reported enzyme-mimetic catalysts. (h) The concentration of Ag^+ released at different times by 1 mL of Ag-V_2O_5 and Ag-V_6O_{13} at a concentration of 10 mg/mL. (i) Dual function of Ag^+ and ROS generation of Ag-V_2O_5.

tetramethylbenzidine (TMB). Fig. 4a demonstrates a correlation between increasing concentrations of Ag-V_2O_5 and the absorbance at 652 nm, indicative of enhanced POD-mimetic activity. Remarkably, Ag-V_2O_5 outperformed V_2O_5, Ag, Ag-V_6O_{13}, and V_6O_{13} in POD-mimetic activity, indicating its superior catalytic ROS-generation performance (Fig. 4b and Fig. S6, Supporting Information). Electron paramagnetic resonance (EPR) analysis revealed that the generated ROS is singlet oxygen ($^1O_2$), with Ag-V_2O_5 producing a significantly higher amount of $^1O_2$ compared to Ag-V_6O_{13} (Fig. 4c). Then, we calculated the initial rate of ROS production (V_0) of Ag-V_2O_5, Ag-V_6O_{13}, and Ag. As illustrated in Fig. 4d, the V_0 of Ag-V_2O_5 is 129.06×10^{-8} Ms^{-1}, greatly exceeding Ag-V_6O_{13} and Ag. By varying the H_2O_2 concentration, the curves of V_0 with respect to H_2O_2 concentration are obtained (Fig. 4e). The Ag-V_2O_5 shows the highest catalytic ROS-production rate across different H_2O_2 concentrations. We further determined the V_{max}, TON, $1/K_m$, and TON/K_m based on the Michaelis-Menten curves (Fig. S7, Supporting Information). As shown in

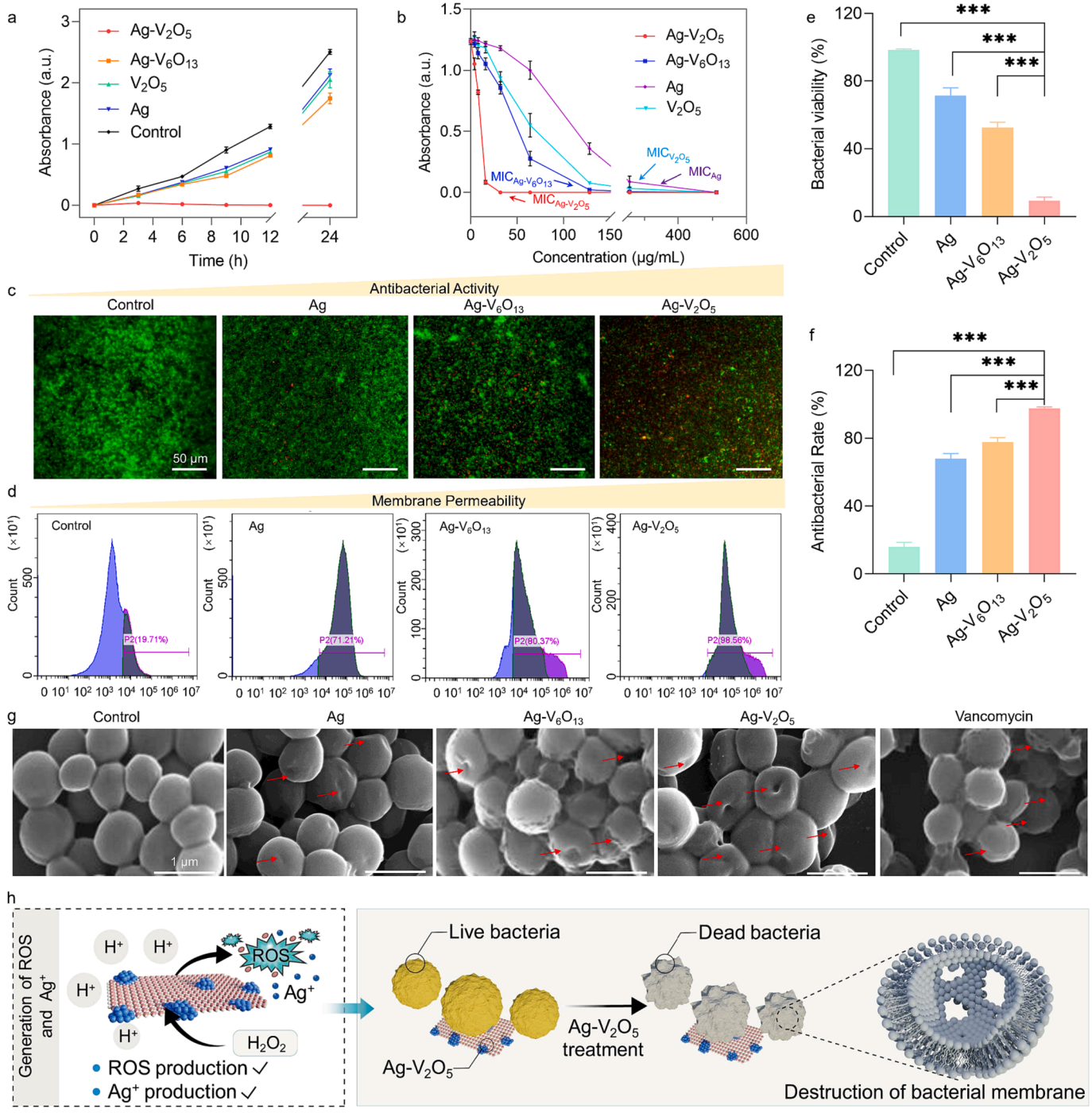

Fig. 5. ***In vitro*** **antibacterial properties of Ag-V_2O_5.** (a-b) OD_{600} values of bare bacteria and the bacteria treated with Ag-V_2O_5, Ag-V_6O_{13}, Ag, and V_2O_5 groups. (c) Live/Dead fluorescent images of the bacteria incubated with Ag-V_2O_5, Ag-V_6O_{13}, Ag, and V_2O_5 groups. (d) Flow cytometry analysis of membrane integrity of Ag-V_2O_5, Ag-V_6O_{13}, Ag, and V_2O_5 treated groups. (e) Bacterial viability of different processing groups calculated by Live/Dead fluorescent staining. (f) Antibacterial rate of different groups calculated by the flow cytometry analysis. (g) SEM images of bacterial sections after Ag-V_2O_5, Ag-V_6O_{13}, and Ag incubation. (h) Schematic diagram of bacterial eradication capability of Ag-V_2O_5. All values are expressed as mean ± SD, n = 6, and p values are assessed by one-way analysis of variance (ANOVA) analysis $^*P < 0.05$, $^{**}P < 0.01$, $^{***}P < 0.001$.

Fig. 4f, Ag-V_2O_5 exhibits the highest V_{max} and TON among the Ag-V_6O_{13} and Ag catalysts, thus confirming its exceptional reactive kinetic of POD-mimetic activity. Although Ag-V_2O_5 did not display the highest $1/K_m$, its TON/K_m, a measure of catalytic efficiency, surpassed those of Ag-V_6O_{13} and Ag. The results indicate that the Ag-V_2O_5 possesses superior catalytic POD-mimetic kinetic and substrates' affinity toward H_2O_2. Furthermore, the V_{max} and TON of Ag-V_2O_5 are 2.66 μM s^{-1} and 200.88×10^{-3} s^{-1}, respectively, surpassing the majority of MOFs, single-atom enzyme mimics, metal oxides, and metal nanoparticles (Fig. 4g and Table S1, Supporting Information).

The kinetics of Ag^+ release were tracked over time using inductively coupled plasma emission spectroscopy (ICP) (Fig. 4h), with Ag-V_2O_5 releasing 0.5 mg/L of Ag^+ by day 5, significantly more than 6 times that of Ag-V_6O_{13}, which only released 0.082 mg/L of Ag^+. Furthermore, the post-release activity of Ag^+ was assessed, revealing a slight decrease in ROS production activity. However, the decline was insignificant, indicating the material's high stability (Fig. S8, Supporting Information). In summary, the prominent V^{5+} presence, combined with a weaker interaction between Ag and V_2O_5, enables Ag-V_2O_5 to exhibit excellent Ag^+ release and ROS generation capabilities, which are crucial for subsequent antimicrobial applications (Fig. 4i).

2.3. Sterilization assessment of drug-resistant bacteria

Pathogenic drug-resistant bacteria pose a significant threat to human life, demanding the development of more effective strategies based on chemotherapies to inhibit these drug-resistant bacteria, an endeavor of the utmost importance for next-generation medicines [54–59]. After discovering the Ag-V_2O_5 heterojunction's remarkable capabilities in ROS and Ag^+ generation, we explored its potential application in neutralizing drug-resistant bacteria. To demonstrate its efficacy, we specifically investigated its activity against the gram-positive *Staphylococcus aureus* (*S. aureus*) and gram-negative *Escherichia coli* (*E. coli*) as representative strains. Various methods, including serial dilution-plate count, optical density (OD_{600}), bacterial mortality assay, and the plotting of bacterial growth curves, were employed. The bacterial concentration was determined using the OD_{600} values obtained from different systems. Our findings reveal that Ag-V_2O_5 exhibits significant antimicrobial activity, outperforming Ag-V_6O_{13}, V_2O_5, and Ag at the same concentrations (Fig. 5a, Fig. S9, Supporting Information). These results were consistent with those obtained from the plate counting method (Fig. S10, Supporting Information). Time-dependent inhibition experiments further revealed that Ag-V_2O_5 completely inhibits bacterial growth during the incubation period, in contrast to the modest antibacterial effects of Ag-V_6O_{13}, V_2O_5, and Ag (Fig. 5a and Fig. S9, Supporting Information). Importantly, the minimum inhibitory concentration (MIC) data highlights Ag-V_2O_5's efficiency, requiring only about 32 μg/mL to achieve close to 100 % inhibition against both *S. aureus* or *E. coli*, significantly lower than the doses required for the other agents (Fig. 5b, Fig. S11, Supporting Information). The minimum bactericidal concentration (MBC) value of the Ag-V_2O_5 system for *S. aureus* and *E. coli* is also found to be 32 μg/mL (Fig. S10, Supporting Information). Meanwhile, we further observed the antibacterial effect of Ag-V_2O_5 after Ag^+ release over 1, 4, and 7 days. Standard plate counting assay results show no obvious decrease in antibacterial capability with Ag^+ release (Fig. S12, Supporting Information). Additionally, Live/Dead bacteria staining revealed that Ag-V_2O_5 has the highest ratio of dead bacteria, with very few viable (green) bacteria observed. In contrast, both the Ag-V_6O_{13} and Ag-treated groups show a significant presence of live bacteria (Fig. 5c and e and Fig. S9, Supporting Information) [60,61]. These results demonstrate the Ag-based microbicide of Ag-V_2O_5 possesses a potent bacterial eradication capacity at an ultralow concentration. Subsequently, the extent of bacterial membrane damage was assessed using PI staining and flow cytometry. The flow cytometry analysis revealed that Ag-V_2O_5 exhibits the highest relative percentage inhibition (PI ratio: 98.56 %) against *S. aureus*, while the Ag-V_6O_{13} and Ag-treated groups show lower values of 80.37 % and 71.21 %, respectively (Fig. 5d and f). Scanning electron microscopy (SEM) imaging showed extensive damage inflicted on bacterial cells, characterized by disrupted and even collapsed bacterial membranes due to treatment with our biocatalysts. In contrast, the untreated bacteria appeared unaffected, with intact cell walls and smooth membranes (Fig. 5g and Fig. S9, Supporting Information). Further study using enlarged SEM imaging revealed that the membrane damage caused by Ag-V_2O_5 is more severe, with membranes appearing more fragmented compared to the Ag-V_6O_{13} and Ag-treated groups. These findings indicate the superior bacterial eradication capability of Ag-V_2O_5, which is associated with the dramatic increase in ROS production and destruction of the bacterial membrane (Fig. 5h). Meanwhile, the increase in bacterial membrane permeability resulted in further permeation by released Ag^+ ions, thereby affecting the intracellular metabolic pathways and triggering bacteria death.

2.4. Healing evaluation of infected wounds in diabetes.

We evaluated the therapeutic potential of Ag-V_2O_5 for treating bacterial-infected wounds in diabetic rats, focusing on its action against *S. aureus* (Fig. 6a and b). The healing process was documented using digital photography (Fig. 6c and Fig. S13, Supporting Information). The residual wound area of each experimental group was then measured to monitor the progress of healing at various stages after the operation (Fig. 6d and Fig. S14, Supporting Information). On day 7, a diabetic wound treated with saline displayed significant tissue swelling and the presence of pus following infection with *S. aureus*. In contrast, the groups treated with Ag-V_2O_5 and vancomycin quickly formed scabs and exhibited reduced swelling and wound sizes. By day 14, the wounds in the Ag-V_2O_5 and vancomycin groups were nearly healed, with smaller scabs, while the saline-treated groups continued to release pus and had larger wound sizes. By day 21, wounds treated with Ag-V_2O_5 or vancomycin were nearly completely healed, in stark contrast with the control group, which still displayed a considerable unhealed area of 33 ±4.15 % of the total wound size. Gross observations indicated that the wounds covered with Ag-V_2O_5 or vancomycin healed significantly faster compared to the saline-treated group throughout the healing process ($P < 0.05$). These findings preliminarily demonstrate that Ag-V_2O_5 exhibits excellent wound disinfection capacity, even at ultralow concentrations (32 μg/mL), and its therapeutic efficacy is comparable to that of vancomycin.

After the wound disinfection treatment, the number of colonies was assessed using the standard plating method. The results indicate that the Ag-V_2O_5 and vancomycin treatments resulted in no visible colonies, whereas the control group showed a significant presence of live bacteria colonies (1069±100 CFU) (Fig. 6e and g). Subsequently, the histological changes in the treated wounds were examined after day 21 using hematoxylin-eosin (H&E) staining. In the control group, a considerable infiltration of granulocytes and neutrophils, as well as the presence of lobulated foreign bodies (marked by black arrows), indicated tissue inflammation due to inadequate protection and the proliferation of microorganisms at the wound sites. In contrast, the Ag-V_2O_5 treated group exhibits a therapeutic effect similar to that of vancomycin, with no infiltration of inflammatory cells and absence of foreign-body reaction (Fig. 6f and Fig. S15, Supporting Information). Additionally, the Ag-V_2O_5 and vancomycin wounds displayed apparent dermal fibroblasts (green arrow), regeneration of hair follicles (red arrows), and a dense structure of granulation tissue. These observations suggest that Ag-V_2O_5 possesses notable wound-healing-accelerating properties by effectively controlling the burden of *S. aureus* and promoting tissue regeneration.

To further analyze wound healing, we used Masson trichrome staining to examine the collagen fibers development on the wound surfaces. This method allows for quantification of the extent of tissue damage and collagen formation in the wound area. Additionally, we used CD31 immunohistochemical staining to identify newly regenerated

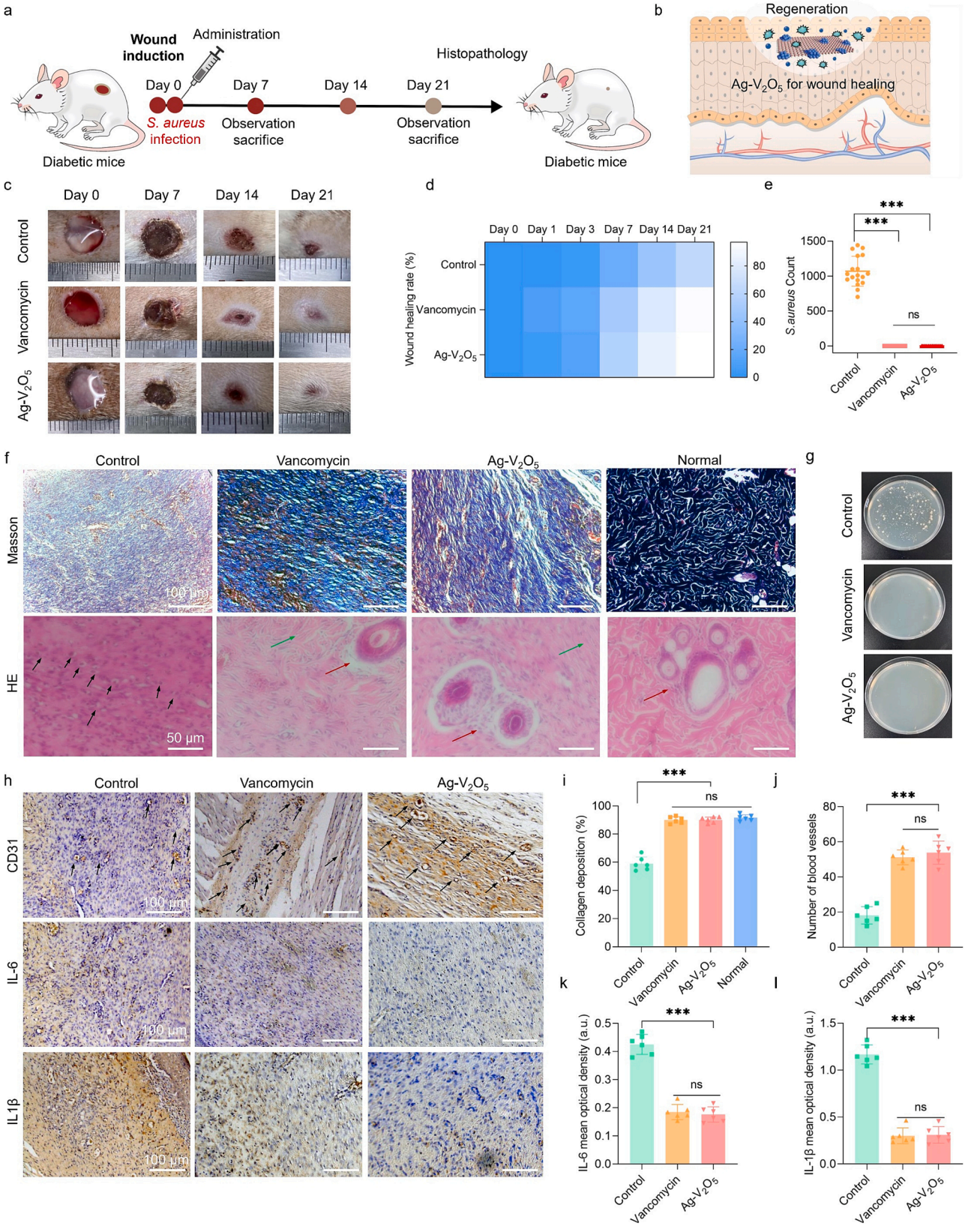

Fig. 6. Healing evaluation of infected wounds in diabetes. (a) Schematic diagram of wound management in diabetic mice. (b) Schematic diagram of Ag-V_2O_5 promoting wound healing in diabetic mice. (c) Digital photographs of the wounds. (d) Time evolution of wound healing rate treated by different systems. (e) The counted *S. aureus* colonies on the plates. (f) Photomicrographs of Masson- and H&E-stained epidermal histological sections after 21 days' posttreatment. (g) Agar plate digital photographs, which are harvested from the Ag-V_2O_5, Vancomycin, and saline-treated wound after 21 days. (h) CD31, IL-6, and IL-1β staining images of the epidermal histological sections after 21 days' posttreatment. (i) Collagen deposition value. (j) Number of CD31 positive blood vessels. (k) IL-6 means optical density. (l) IL-1β means optical density. Asterisks indicate significant differences (*$P < 0.05$, **$P < 0.01$, ***$P < 0.001$), ns. represents no significant differences. All values are expressed as mean ± SD ($n = 5$), P values are assessed by ANOVA analysis.

endothelial cells, which serve as markers for angiogenesis following revascularization in the infected wound sites [62]. As shown in Fig. 6f and i, the regeneration of damaged tissue was observed to be significantly enhanced in the Ag-V_2O_5 (92±5 %) and vancomycin (96±2 %) groups, as indicated by the large presence of collagen occupying the tissue slices. This collagen distribution pattern is comparable to that of healthy skin. Furthermore, the homogeneous distribution pattern and well-formed collagen fibers in the wound sites indicate a higher level of collagen formation, in stark contrast to the control group. Moreover, the Ag-V_2O_5 (54±6) and vancomycin groups (51±4) exhibit intense staining of CD31, suggesting a greater occurrence of neovascularization (indicated by black arrows) when compared to the control group (18±5) (Fig. 6h and j). These findings indicate that Ag-V_2O_5 not only supports but also accelerates the wound healing process by promoting angiogenesis and vasculogenesis, critical steps toward successful tissue repair and regeneration.

Chronic inflammation is a major barrier to wound healing in individuals with diabetes [63]. To assess the inflammation within infected wounds in diabetic patients, we measured the levels of key inflammatory markers. Untreated diabetic wounds showed significantly higher levels of cytokines like IL-6 and IL-1β in comparison to wounds treated with Ag-V_2O_5 or vancomycin (Fig. 6j–l). During the initial stages of wound infection, the production of these pro-inflammatory cytokines stimulates immune cells, triggering an inflammatory cascade response. The application of Ag-V_2O_5 was associated with a noticeable reduction in IL-6 and IL-1β levels, indicating not only its antimicrobial efficacy but also its potential to modulate the inflammatory response, thus promoting a more conducive environment for wound healing in diabetic patients.

To determine the biocompatibility of Ag-V_2O_5, we used human umbilical vein endothelial cells (HUVECs) as a cellular model. The results clearly demonstrate that Ag-V_2O_5 exhibits minimal cytotoxicity (Figs. S16-S17, Supporting Information). Fluorescence imaging and cell counting kit-8 detected no induction of early apoptosis by Ag-V_2O_5, even at relatively high concentrations of 64 μg/mL. CCK8 assay to detect cell proliferation showed that HUVECs growth retardation under the high-glucose culture and growth more rapid in Ag-V_2O_5 (Fig. S19, Supporting Information). In addition to the cell compatibility study, histological examinations were conducted to evaluate the potential systemic toxicity of Ag-V_2O_5 on vital organs. Histopathological analyses of the heart, liver, spleen, lungs, and kidneys from treated subjects revealed no evidence of damage or noticeable abnormalities in comparison to control rats. The absence of histological anomalies, as shown in Fig. S18, Supporting Information, supports the conclusion that Ag-V_2O_5 does not exert cumulative toxicity, indicating excellent biosafety for potential therapeutic use.

3. Conclusion

In summary, our findings indicate that enzymatic Ag-V_2O_5 heterojunctions, with mutually reinforced bifunctional chemotherapies, emerge as an ideal material for combating drug-resistant bacterial infections. This efficacy is largely due to the complete occupation of V^{5+} electron orbitals, which impedes the capture of electrons from Ag by V via bridging oxygen bonds, thus minimizing the interaction between Ag and V_2O_5. As a result, Ag-V_2O_5 exhibits excellent Ag^+ release and ROS generation abilities, making it a promising candidate for treating and healing wound infections. Notably, Ag-V_2O_5 exhibits a potent antibacterial activity, evidenced by a low inhibitory concentration (32 μg/mL Ag-V_2O_5) against *S. aureus*, and possesses the ability to effectively promote wound healing by *in vivo* disinfection of rat skin. The novel approach of bifunctional chemotherapies on valence-modulated Ag^+ release and ROS-catalysis not only represents a significant step forward in the development of chronic wound therapy but also has the potential to inspire further discoveries in Ag^+ and ROS-based biomedical therapeutics.

4. Experimental section

Experimental details, including materials, characterizations, synthesis, POD-mimetic kinetic assays, EPR measurement, antibacterial experiments, *in vitro* cytotoxicity, and wound healing examination, are listed in the Supporting Information.

Author contributions

Q.Z. and T.W. contributed equally to this work. Q.Z. and T.W. performed the experiments and analyzed the results. Z.Y.X. performed the theoretical calculations. Q.Z., T.W., R.D.R., and L.C. assisted with the figure production and experimental design. Q.Z., T.W., R.D.R., L.C., Y. G., Q.C., and C.C. wrote the manuscript. Y.G., Q.C., and C.C. designed the experiments, corrected the manuscript, and supervised the whole project. All authors discussed the results and commented on the manuscript.

CRediT authorship contribution statement

Qian Zhou: Investigation, Methodology, Writing – original draft, Writing – review & editing. **Ting Wang:** Investigation, Methodology, Writing – original draft, Writing – review & editing. **Zhenyu Xing:** Methodology, Software. **Raul D. Rodriguez:** Conceptualization, Data curation, Writing – original draft. **Liang Cheng:** Data curation, Validation, Methodology. **Yang Gao:** Data curation, Methodology, Supervision, Resources. **Qiu Chen:** Methodology, Resources, Validation, Conceptualization. **Chong Cheng:** Conceptualization, Funding acquisition, Resources, Writing – original draft, Writing – review & editing.

Declaration of competing interest

The authors declare that they have no known competing financial interests or personal relationships that could have appeared to influence the work reported in this paper.

Data availability

Data will be made available on request.

Acknowledgments

This work was financially supported by the National Key R&D Program of China (2019YFA0110600 and 2021YFB3800705), National Natural Science Foundation of China (Nos. 52161145402 and 52173133), the Science and Technology Project of Sichuan Province (Nos. 2023YFH0008 and 2023YFS0019), and 1·3·5 Project for Disciplines of Excellence, West China Hospital, Sichuan University (No. ZYJC21047).

Appendix A. Supplementary data

Supplementary data to this article can be found online at https://doi.org/10.1016/j.cej.2024.149249.

References

[1] Y. Deng, Y. Gao, T. Li, S. Xiao, M. Adeli, et al., Amorphizing metal selenides-based ros biocatalysts at surface nanolayer toward ultrafast inflammatory diabetic wound healing, ACS Nano 17 (2023) 2943–2957.
[2] P.P. Rade, P.S. Giram, A.A. Shitole, N. Sharma, B. Garnaik, Physicochemical and in vitro antibacterial evaluation of metronidazole loaded eudragit s-100 nanofibrous mats for the intestinal drug delivery, Adv. Fiber Mater. 4 (2021) 76–88.
[3] Y. Dang, J. Guan, Nanoparticle-based drug delivery systems for cancer therapy, Smart Mater. Med. 1 (2020) 10–19.
[4] Q. Gao, Q. Bai, C. Zheng, N. Sun, J. Liu, et al., Application of metal-organic framework in diagnosis and treatment of diabetes, Biomolecules 12 (2022) 1240.
[5] S. Cao, Z. Zhao, Y. Zheng, Z. Wu, T. Ma, et al., A library of ros-catalytic metalloenzyme mimics with atomic metal centers, Adv. Mater. 34 (2022) 2200255.

[6] Y. Qiao, X. Liu, B. Li, Y. Han, Y. Zheng, et al., Treatment of mrsa-infected osteomyelitis using bacterial capturing, magnetically targeted composites with microwave-assisted bacterial killing, Nat. Commun. 11 (2020) 4446.
[7] F. Huang, X. Cai, X. Hou, Y. Zhang, J. Liu, et al., A dynamic covalent polymeric antimicrobial for conquering drug-resistant bacterial infection, Exploration 2 (2022) 20210145.
[8] Y.K. Wu, N.C. Cheng, C.M. Cheng, Biofilms in chronic wounds: Pathogenesis and diagnosis, Trends Biotechnol. 37 (2019) 505–517.
[9] W.J. Jeffcoate, K.G. Harding, Diabetic foot ulcers, Lancet 361 (2003) 1545–1551.
[10] J. Guo, Z. Xing, L. Liu, Y. Sun, H. Zhou, et al., Antioxidase-like nanobiocatalysts with ultrafast and reversible redox-centers to secure stem cells and periodontal tissues, Adv. Funct. Mater. 33 (2023) 2211778.
[11] X. Xiang, X. Feng, S. Lu, B. Jiang, D. Hao, et al., Indocyanine green potentiated paclitaxel nanoprodrugs for imaging and chemotherapy, Exploration 2 (2022) 20220008.
[12] K. Järbrink, G. Ni, H. Sönnergren, A. Schmidtchen, C. Pang, et al., The humanistic and economic burden of chronic wounds: A protocol for a systematic review, Syst. Rev. 6 (2017) 15.
[13] G. Dabiri, E. Damstetter, T. Phillips, Choosing a wound dressing based on common wound characteristics, Adv. Wound Care (new Rochelle) 5 (2016) 32–41.
[14] A. Gefen, How medical engineering has changed our understanding of chronic wounds and future prospects, Med. Eng. Phys. 72 (2019) 13–18.
[15] K.F. Cutting, Wound exudate: Composition and functions, Br. J. Community Nurs. 8 (2003) 4–9.
[16] X. Wu, S. Xiao, Y. Long, T. Ma, W. Shao, et al., Emerging 2d materials for electrocatalytic applications: Synthesis, multifaceted nanostructures, and catalytic center design, Small 18 (2022) 2105831.
[17] N. Rodríguez-Rodríguez, I. Martínez-Jiménez, A. García-Ojalvo, Y. Mendoza-Mari, G. Guillén-Nieto, et al., Wound chronicity, impaired immunity and infection in diabetic patients, MEDICC REV. 24 (2022) 44–58.
[18] N. Lv, Q. Li, H. Zhu, S. Mu, X. Luo, et al., Electrocatalytic porphyrin/phthalocyanine-based organic frameworks: Building blocks, coordination microenvironments, structure-performance relationships, Adv. Sci. 10 (2023) 2206239.
[19] Z. Wu, Y. Sun, S. Mu, M. Bai, Q. Li, et al., Manganese-based antioxidase-inspired biocatalysts with axial Mn−N5 sites and 2d d-π-conjugated networks for rescuing stem cell fate, Angew. Chem. Int. Ed. 62 (2023) e202302329.
[20] Y. Xia, H. Yang, S. Li, S. Zhou, L. Wang, et al., Multivalent polyanionic 2d nanosheets functionalized nanofibrous stem cell-based neural scaffolds, Adv. Funct. Mater. 31 (2021) 2010145.
[21] J.S. Chin, L. Madden, S.Y. Chew, D.L. Becker, Drug therapies and delivery mechanisms to treat perturbed skin wound healing, Adv. Drug Delivery Rev. 149–150 (2019) 2–18.
[22] K. Chen, F. Wang, S. Liu, X. Wu, L. Xu, et al., In situ reduction of silver nanoparticles by sodium alginate to obtain silver-loaded composite wound dressing with enhanced mechanical and antimicrobial property, Int. J. Biol. Macromol. 148 (2020) 501–509.
[23] L. Ma, F. Jiang, X. Fan, L. Wang, C. He, et al., Metal–organic-framework-engineered enzyme-mimetic catalysts, Adv. Mater. 32 (2020) 2003065.
[24] C. Gong, W. Guan, X. Liu, Y. Zheng, Z. Li, et al., Biomimetic bacteriophage-like particles formed from probiotic extracts and no donors for eradicating multidrug-resistant staphylococcus aureus, Adv. Mater. 34 (2022) 2206134.
[25] Y. Lv, C. Chen, L. Jin, Y. Zheng, S. Wu, et al., Microwave-excited, antibacterial core-shell $BaSO_4/BaTi_5O_{11}$@ppy heterostructures for rapid treatment of s, Aureus-Infected Osteomyelitis, Acta Biomater. 167 (2023) 506–518.
[26] Y. Opoku-Damoah, R. Zhang, H.T. Ta, Z.P. Xu, Therapeutic gas-releasing nanomedicines with controlled release: Advances and perspectives, Exploration 2 (2022) 20210181.
[27] C. Wu, Z. Zhang, K. Zhou, W. Chen, J. Tao, et al., Preparation and characterization of borosilicate-bioglass-incorporated sodium alginate composite wound dressing for accelerated full-thickness skin wound healing, Biomed. Mater. 18 (2020) 055009.
[28] L. Wang, J. Yang, X. Yang, Q. Hou, S. Liu, et al., Mercaptophenylboronic acid-activated gold nanoparticles as nanoantibiotics against multidrug-resistant bacteria, ACS Appl. Mater. Interfaces 12 (2020) 51148–51159.
[29] T. Chen, Y. Chen, H.U. Rehman, Z. Chen, Z. Yang, et al., Ultratough, self-healing, and tissue-adhesive hydrogel for wound dressing, ACS Appl. Mater. Interfaces 10 (2018) 33523–33531.
[30] M. He, L. Sun, X. Fu, S.P. McDonough, C.C. Chu, Biodegradable amino acid-based poly(ester amine) with tunable immunomodulating properties and their in vitro and in vivo wound healing studies in diabetic rats' wounds, Acta Biomater. 84 (2019) 114–132.
[31] L.I. Moura, A.M. Dias, E. Carvalho, H.C. de Sousa, Recent advances on the development of wound dressings for diabetic foot ulcer treatment, Acta Biomater. 9 (2013) 7093–7114.
[32] S. Mu, Y. Deng, Z. Xing, X. Rong, C. He, et al., Ir cluster-anchored mofs as peroxidase-mimetic nanoreactors for diagnosing hydrogen peroxide-related biomarkers, ACS Appl. Mater. Interfaces 14 (2022) 56635–56643.
[33] V. Tzaneva, I. Mladenova, G. Todorova, D. Petkov, Antibiotic treatment and resistance in chronic wounds of vascular origin, Clujul Med. 89 (2016) 365–370.
[34] Y. Sun, S. Mu, Z. Xing, J. Guo, Z. Wu, et al., Catalase-mimetic artificial biocatalysts with ru catalytic centers for ros elimination and stem-cell protection, Adv. Mater. 34 (2022) 2206208.
[35] Y. Yan, Z. Liu, T. Wan, W. Li, Z. Qiu, et al., Bioinspired design of na-ion conduction channels in covalent organic frameworks for quasi-solid-state sodium batteries, Nat. Commun. 14 (2023) 3066.
[36] C. Nie, C. Cheng, Z. Peng, L. Ma, C. He, et al., Mussel-inspired coatings on ag nanoparticle-conjugated carbon nanotubes: Bactericidal activity and mammal cell toxicity, J. Mater. Chem. B 4 (2016) 2749–2756.
[37] D. Leaper, O. Assadian, C.E. Edmiston, Approach to chronic wound infections, Br. J. Dermatol. 173 (2015) 351–358.
[38] C. Willyard, The drug-resistant bacteria that pose the greatest health threats, Nature 543 (2017) 15.
[39] L. Wang, B. Zhu, Y. Deng, T. Li, Q. Tian, et al., Biocatalytic and antioxidant nanostructures for ros scavenging and biotherapeutics, Adv. Funct. Mater. 31 (2021) 2101804.
[40] T. Wang, W. Wang, W. Shao, M. Bai, M. Zhou, et al., Synthesis and electronic modulation of nanostructured layered double hydroxides for efficient electrochemical oxygen evolution, ChemSusChem 14 (2021) 5112–5134.
[41] N. Zhang, X. Zhang, L. Tao, P. Jiang, C. Ye, et al., Silver single-atom catalyst for efficient electrochemical CO2 reduction synthesized from thermal transformation and surface reconstruction, Angew. Chem. Int. Ed. 60 (2021) 6170–6176.
[42] D.D. Gao, X.H. Wu, P. Wang, H.G. Yu, B.C. Zhu, et al., Selenium-enriched amorphous NiSe1+x nanoclusters as a highly efficient cocatalyst for photocatalytic H2 evolution, Chem. Eng. J. 408 (2021) 127230.
[43] S. Wang, J. Li, Y. Cao, J. Gu, Y. Wang, et al., Non-leaching, rapid bactericidal and biocompatible polyester fabrics finished with benzophenone terminated n-halamine, Adv. Fiber Mater. 4 (2021) 119–128.
[44] Y. Zhou, J. Wu, Y. Li, W. Zhang, Y. Zou, et al., Fabrication of sulfated silk fibroin-based blend nanofibrous membranes for lysozyme adsorption, Adv. Fiber Mater. 4 (2021) 89–97.
[45] M. Cao, S. Wang, J.H. Hu, B.H. Lu, Q.Y. Wang, et al., Silver cluster-porphyrin-assembled materials as advanced bioprotective materials for combating superbacteria, Adv. Sci. 9 (2021) 2103721.
[46] T. Bruna, F. Maldonado-Bravo, P. Jara, N. Caro, Silver nanoparticles and their antibacterial applications, Int. J. Mol. Sci. 22 (2021) 7202.
[47] P. Wang, H. Yang, C. Tang, Y. Wu, Y. Zheng, et al., Boosting electrocatalytic CO2–to–ethanol production via asymmetric C-C coupling, Nat. Commun. 13 (2022) 3754.
[48] A. Ivask, A. Elbadawy, C. Kaweeteerawat, D. Boren, H. Fischer, et al., Toxicity mechanisms in escherichia coli vary for silver nanoparticles and differ from ionic silver, ACS Nano 8 (2014) 374–386.
[49] J.T. Seil, T.J. Webster, Antimicrobial applications of nanotechnology: Methods and literature, Int. J. Nanomedicine 7 (2012) 2767–2781.
[50] M.A. Quinteros, V. Cano Aristizábal, P.R. Dalmasso, M.G. Paraje, P.L. Páez, Oxidative stress generation of silver nanoparticles in three bacterial genera and its relationship with the antimicrobial activity, Toxicol. in Vitro 36 (2016) 216–223.
[51] Y. Ding, G. Ren, G. Wang, M. Lu, J. Liu, et al., V_2O_5 nanobelts mimick tandem enzymes to achieve nonenzymatic online monitoring of glucose in living rat brain, Anal. Chem. 92 (2020) 4583–4591.
[52] X. Wang, S. Li, L. Zhao, C. Xu, J. Gao, A dft and td-dft study on electronic structures and uv-spectra properties of octaethyl-porphyrin with different central metals(Ni, V, Cu, Co), Chin. J. Chem. Eng. 28 (2020) 532–540.
[53] S. Ghosh, P. Roy, N. Karmodak, E.D. Jemmis, G. Mugesh, Nanoisozymes: Crystal-facet-dependent enzyme-mimetic activity of V2O5 nanomaterials, Angew. Chem. Int. Ed. 57 (2018) 4510–4515.
[54] S. Shen, M. Mamat, S. Zhang, J. Cao, Z.D. Hood, et al., Synthesis of CaO_2 nanocrystals and their spherical aggregates with uniform sizes for use as a biodegradable bacteriostatic agent, Small 15 (2019) 1902118.
[55] R. Wang, B. Liu, S. You, Y. Li, Y. Zhang, et al., Three-dimensional Ni_3Se_4 flowers integrated with ultrathin carbon layer with strong electronic interactions for boosting oxygen reduction/evolution reactions, Chem. Eng. J. 430 (2022) 132720.
[56] Y. Long, L. Li, T. Xu, X. Wu, Y. Gao, et al., Hedgehog artificial macrophage with atomic-catalytic centers to combat drug-resistant bacteria, Nat. Commun. 12 (2021) 6143.
[57] Y. Yang, Y. Du, J. Zhang, H. Zhang, B. Guo, Structural and functional design of electrospun nanofibers for hemostasis and wound healing, Adv. Fiber Mater. 4 (2022) 1027–1057.
[58] W. Yang, H. Ding, D. Puglia, J.M. Kenny, T. Liu, et al., Bio-renewable polymers based on lignin-derived phenol monomers: Synthesis, applications, and perspectives, Susmat 2 (2022) 535–568.
[59] Y. Xie, S. Xiao, L. Huang, J. Guo, M. Bai, et al., Cascade and ultrafast artificial antioxidases alleviate inflammation and bone resorption in periodontitis, ACS Nano 17 (2023) 15097–15112.
[60] L. Wang, F. Gao, A. Wang, X. Chen, H. Li, et al., Defect-rich adhesive molybdenum disulfide/rgo vertical heterostructures with enhanced nanozyme activity for smart bacterial killing application, Adv. Mater. 32 (2020) 2005423.
[61] Z. Xu, Z. Qiu, Q. Liu, Y. Huang, D. Li, et al., Converting organosulfur compounds to inorganic polysulfides against resistant bacterial infections, Nat. Commun. 9 (2018) 3713.
[62] W.A.M. Steven, M. Albelda, ClaytonA. Buck, Peter J. Newmanl, Molecular and cellular properties of pecam-1(endocam/cd31): A novel vascular cell-cell adhesion molecule, J. Cell Biol. 114 (1991) 1059–1068.
[63] P. Martin, R. Nunan, Cellular and molecular mechanisms of repair in acute and chronic wound healing, Br. J. Dermatol. 173 (2015) 370–378.